Anchoring effect of distorted octahedra on the stability and strength of platinum metal pernitrides

Z. H. Fu,[1,2] T. G. Bi,[3] S. H. Zhang,[1,2] S. Chen,[1,2] E. Zurek,[3] D. Legut,[4] T. C. Germann,[5] T. Lookman,[5] and R. F. Zhang[1,2,*]

[1]*School of Materials Science and Engineering, Beihang University, Beijing 100191, People's Republic of China*

[2]*Center for Integrated Computational Materials Engineering (International Research Institute for Multidisciplinary Science) and Key Laboratory of High-Temperature Structural Materials and Coatings Technology (Ministry of Industry and Information Technology), Beihang University, Beijing 100191, People's Republic of China*

[3]*Department of Chemistry, State University of New York at Buffalo, Buffalo, New York 14260-3000, USA*

[4]*IT4Innovations and Nanotechnology Centre, VSB-Technical University of Ostrava, CZ-70833 Ostrava, Czech Republic*

[5]*Theoretical Division, Los Alamos National Laboratory, Los Alamos, New Mexico 87545, USA*

(Received 12 September 2018; published 8 January 2019)

The successful preparation of platinum metal pernitrides (PmN_2) in high-temperature and high-pressure experiments has aroused great scientific interest, since it has long been thought that these systems could not be prepared, and also because of their intriguing mechanical properties. Although it is now widely recognized that PmN_2 phases can be stabilized under high pressure, the physical origin explaining their stability remains unknown. By means of high-throughput first-principles schemes, we reveal that the choice of specific space group of these pernitrides at high pressure can be quantified by the anchoring effect of distorted PmN_6 octahedra. The competition between baddeleyite and marcasite is attributed uniquely to Pm dimerization, resulting in a profound enhancement of Pm-Pm bonding and N-N π antibonding, while Pm-N bonding plays a secondary role. The observed mechanical strength and atomic deformation mechanism of PmN_2 suggest that they are ultraincompressible yet soft. This is attributed to the breaking of elongated Pm-N bonds in the PmN_6 octahedra, which is accompanied by a continuous semiconductor-semimetal-metal transition for the semiconducting PmN_2 during straining. These findings shed light on the physical origin of high-pressure stabilization and highlight the importance of exploring deformation mechanisms in designing novel strong solids.

DOI: 10.1103/PhysRevMaterials.3.013603

I. INTRODUCTION

It was long believed that the platinum-metal (Pm) elements (i.e., Pt, Ir, Os, Pd, Rh, and Ru) are unable to form stable compounds with nitrogen at ambient conditions, but their pernitrides (PmN_2) have now been successfully synthesized under high pressure and high temperature [1–4]. By now experiments and theory have reached a consensus concerning the observed crystal structures and stoichiometry of PmN_2 [5–8]. PtN_2 forms the pyrite structure, which is a cubic phase with the Pt atom occupying the fcc site and its surrounding six nitrogen atoms forming a corner-sharing octahedron [5]. A rotation of the distorted PmN_6 octahedra results in the marcasite structure for OsN_2 [9], and yields the baddeleyite ($CoSb_2$) structure of IrN_2 [10]. On the basis of a permutation and a combinatorial strategy of the specific sites in the fcc lattice in a 12-atom conventional cell, the thermodynamic stability of all analogs of the aforementioned structures was explored [6], followed by crystal structure prediction using an evolutionary methodology [11]. Despite the fact that several new low-energy layered crystal structures were proposed, only the three classical structures (pyrite, marcasite, and baddeleyite) have been experimentally confirmed, and thus structural dependence on the composition motivates us to explore the physical origin of the structural preference for each PmN_2.

The stabilization in pyrite-type PtN_2 was originally attributed to the anchoring effect of strong covalent N-N bonds [1–3,5]. However, it cannot explain the structures of the other pernitrides in view of the fact that the N-N bond lengths (1.40 Å for OsN_2, 1.42 Å for IrN_2, and 1.42 Å for PtN_2) are nearly the same in the various structures. Later on, a Peierls mechanism [12] was proposed to be the origin of the stabilization for the marcasite to baddeleyite transition in IrN_2 [10]. However, this mechanism cannot elucidate the stabilization of higher-symmetrical structures for OsN_2 and PtN_2 because both the marcasite and pyrite structures are metallic [9]. Therefore, a universal electronic origin of the structural stability has not yet been uncovered.

Since the discovery of the PmN_2 phases their intriguing mechanical properties such as ultrahigh elastic moduli (428 GPa for IrN_2 [3], 358 GPa for OsN_2 [3], and 354 GPa for PtN_2 [1]) and unique electronic structures, e.g., band gaps of ∼2 eV for PtN_2 [5] and ∼0.4 eV for IrN_2 [10], have been intensely studied. Moreover, it was proposed that these phases have the potential to be superhard materials [2,3]. By reinforcing the PmN_6 octahedra, the strong covalent N-N bonding was originally thought to result in a strengthening effect in the pernitrides, paving a way for designing strong solids [10,13,14]. However, investigations on transition-metal (Tm) nitrides indicate that the weak Tm-N bonds are responsible for the irreversible plastic deformation [15–17], and therefore the

*Corresponding author: zrf@buaa.edu.cn

strengthening effect of N-N bonds is questionable since the weakest link (e.g., Pm-N and Pm-Pm) would make the lattice instability occur under much lower stress before breaking the N-N bonds [8]. In this paper, a detailed investigation on the anisotropic ideal strengths and atomic deformation paths indicates surprisingly that instead of the strong N-N bonds the weak Pm-N bonds in the distorted PmN_6 octahedra carry the plastic flow, thereby shedding light on the origin of the weakness of PmN_2.

II. COMPUTATIONAL METHODS

The present density functional theory calculations were performed using the Vienna *Ab-Initio* Simulation Package (VASP) [18] with the projector augmented wave (PAW) basis [19] employed to describe the electron-ion interaction and the Perdew, Burke, and Ernzerhof (PBE) exchange-correlation functional [20] for the exchange-correlation term. The kinetic-energy cutoff of 600 eV and the Monkhorst-Pack k-mesh grids of 8000 k points per reciprocal atom [21,22] were adopted for the stress calculations. The phonon dispersions were calculated using the PHONOPY code coupled with VASP [23]. Crystal orbital Hamilton populations (COHP) analyses were done using the LOBSTER code [24]. The elastic properties were calculated via the AELAS code [22]. The lattice constants along with the polycrystalline Voigt shear (G_V) and bulk (B_V) moduli were obtained using the Voigt-Reuss-Hill approximation [25,26].

During the calculation of stress-strain relationships under tensile loading, the simulated cell was projected onto a Cartesian coordinate system with one crystallographic direction parallel to a Cartesian axis along which the tension loading was applied. In case of shear deformation, one Cartesian axis was chosen normal to the slip plane and the other Cartesian axis was chosen parallel to the slip direction. The simulated cell was incrementally deformed by a transformation of the unstrained cell vector to the strained ones by multiplying the deformation matrices. Afterwards, an ionic relaxation was performed to make both the specific lattice vectors and the ionic coordinates relaxed by fixing the applied strain component while relaxing the other five strain components, until their conjugate stress components, i.e., Hellmann-Feynman stresses, reached less than 0.1 GPa.

Evolutionary structure searches were performed using the open-source evolutionary algorithm (EA) XtalOpt [27,28] along with the default parameter set from Ref. [27]. EA runs were carried out on the Pm pernitrides with two, three, and four formula units in the primitive cell. In this algorithm a new offspring was created as soon as an individual was optimized and the parents were chosen from a population based pool. The population sizes were around 735, 225, and 110 for the two, three, and four formula unit cells of the Pm pernitrides, respectively. In each run the same low enthalpy structure was found at least three times (often more) before the run was terminated. A four-step structural-optimization scheme was used for all runs, and each step employed the geometry of the structure from the previous step for the initial geometry. Only the ions were allowed to relax in the first step, while the last three steps also allowed the lattice parameters to relax. The precision of the calculation was increased at each step. The calculations were performed using the PBE exchange-correlation functional, the PAW method, and an energy cutoff of 500 eV in the final step. The lowest-energy structures from each search were optimized using the aforementioned computational settings, to obtain a more accurate energy ranking.

III. RESULTS AND DISCUSSION

We first searched for the most stable structures of PmN_2 at 0 and 50 GPa by means of high-throughput screening based on the Inorganic Crystal Structure Database (ICSD) prototype library via the VASP code [18]. In total, there are about 300 prototypes with chemical stoichiometry of AB_2 or A_2B provided in the ICSD [29]. In our paper we only consider the 265 structures that have less than 35 atoms in the unit cell (the details of the structures are listed in Table S1 in Supplemental Material [30]). To the best of our knowledge, this is the largest structural prototype library used in high-throughput computations (note: ∼10 and ∼100 prototype structures are considered for AB_2/A_2B compounds within aflowlib [31] and OQMD [32], respectively). Figures 1(a)–1(c) shows the calculated formation enthalpies of the 265 prototype structures for OsN_2, IrN_2, and PtN_2 at 0 and 50 GPa. It is observed that two layered structures have the lowest formation enthalpies for PmN_2 at 0 GPa, including the simple tetragonal structure belonging to space group 127 ($P4/mbm$) for PtN_2 and the simple hexagonal structure with space group 191 ($P6/mmm$) for OsN_2 and IrN_2. Note that all of these layered structures have also been confirmed by our evolutionary structure searches [27,28]. Although it was proposed that these layered structures could be quenched to atmospheric conditions by phase transformations from structures synthesized under pressure [11,33], all of them are thermodynamically unstable with respect to decomposition into elemental Pm and α-N_2, in agreement with the fact that they have not been synthesized so far. At 50 GPa, we found that three high-pressure structures [see Figs. 1(d)–1(f)], including marcasite, baddeleyite, and pyrite, are the most stable for OsN_2, IrN_2, and PtN_2, respectively. The calculated formation enthalpies for all of the pernitrides are negative (−0.54 eV/atom for OsN_2, −0.64 eV/atom for IrN_2, and −0.68 eV/atom for PtN_2), suggesting their thermodynamically feasibility at high pressure. These findings lead to two critical questions.

(i) Since the formation enthalpies of these pernitrides in the marcasite and baddeleyite structures are comparable, why does OsN_2 adopt the marcasite structure, while IrN_2 prefers the baddeleyite structure?

(ii) What is the electronic origin of the stabilization of the pyrite structure for PtN_2?

Before answering these questions, the dynamic stabilities of the three structures are explored by analyzing the high-pressure phonon dispersions (shown in Fig. S1 in Supplemental Material [30]). A significant soft mode appears at the T (0.5, 0, 0.5) point in marcasite-type IrN_2, which indicates a cell-doubling phase transition, corresponding to the emergence of the baddeleyite structure, in agreement with a previous report [10]. The basis vectors of the marcasite structure ($\vec{a}$, $\vec{b}$, $\vec{c}$) correspond to the $[10\bar{1}]/2$, [010], and [101]/2 crystal

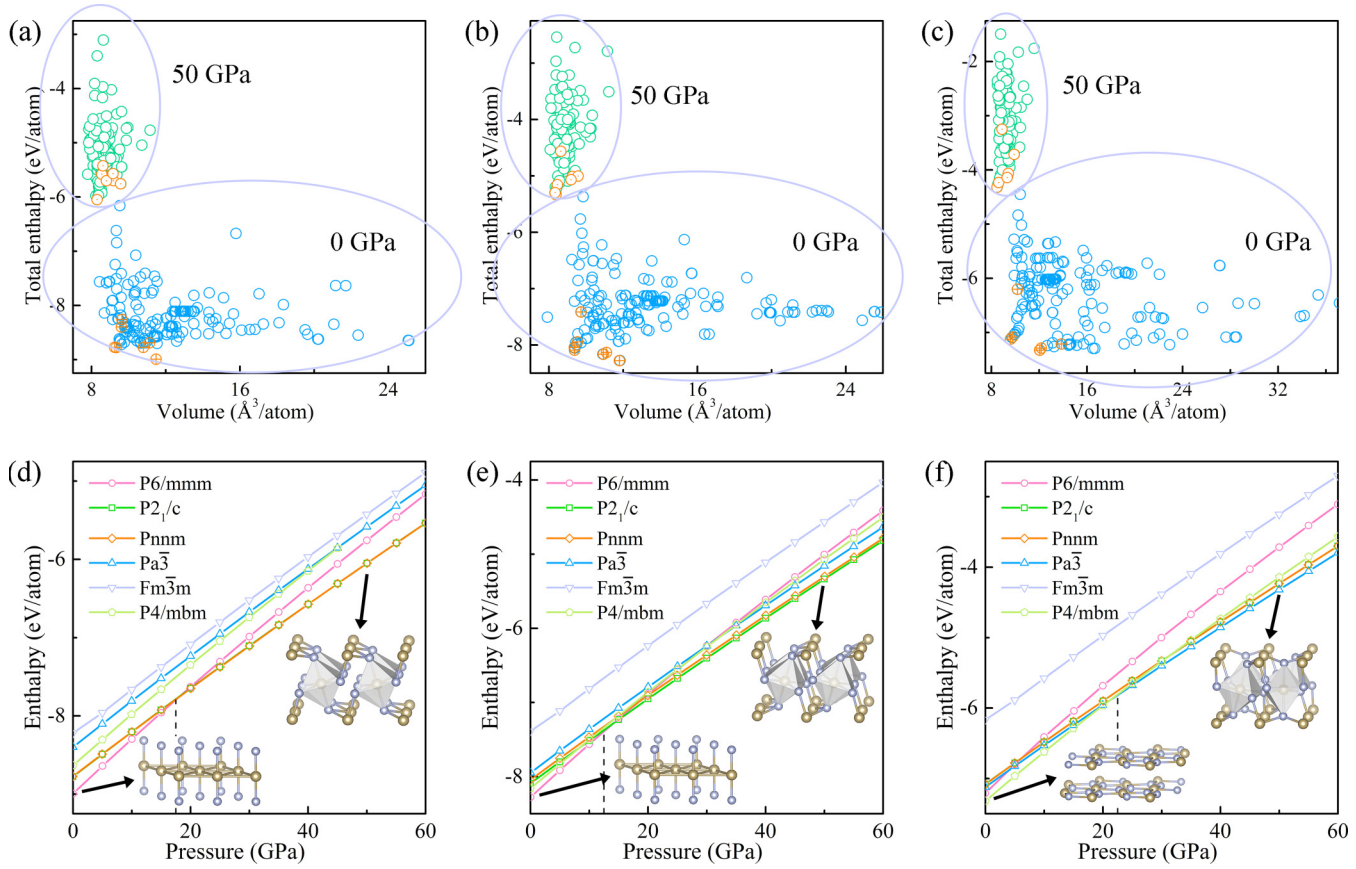

FIG. 1. The high-throughput screening of the most stable structures of (a) OsN_2, (b) IrN_2, and (c) PtN_2 according to the 265 crystallographic structure prototypes collected in the ICSD library. (d)–(f) The enthalpy-pressure relationships of (d) OsN_2, (e) IrN_2, and (f) PtN_2 in six selected structures, i.e., simple hexagonal ($P6/mmm$), baddeleyite ($P2_1/c$), marcasite ($Pnnm$), pyrite (Pa-3), cubic (Fm-3m), and simple tetragonal ($P4/mbm$).

orientations of the baddeleyite structure, respectively. The angle (90.51° at 50 GPa) between the [10$\bar{1}$] and [101] crystal orientations of the baddeleyite-type IrN_2 structure has only a small deviation (0.51°) from the corresponding angle in the marcasite structure. Both baddeleyite-type and marcasite-type OsN_2 are dynamically stable, whereas the acoustic branches of the latter have larger slopes around the Γ point, suggesting a larger elastic stiffness. For PtN_2, the absence of imaginary modes indicates the dynamic stabilities of the baddeleyite, marcasite, and pyrite structures, while pyrite-type PtN_2 is favored because of its lowest formation enthalpy.

To investigate the relative stabilities of OsN_2 and IrN_2 in different structure types at 50 GPa more clearly, hypothetical structures containing elements from the left-hand side of the periodic table, WN_2 and ReN_2, and the right-hand side of the periodic table, AuN_2 and HgN_2, with three structure types have also been included for comparison. Besides the formation enthalpy, ΔH, we have considered the PV term in enthalpy, PV, and the N-N bond length, $d_{\text{N-N}}$, as additional descriptors [see Fig. 2(a)]. Similar to IrN_2, both WN_2 and ReN_2 with baddeleyite-type structures have the lowest ΔH among the three structure types. The too positive ΔH makes it unlikely that the three phases of AuN_2 and HgN_2 will be synthesized experimentally [34]. The enthalpy, H, is defined as $H = U + PV$, where U, P, and V are the internal energy, pressure, and volume per formula unit, respectively. Interestingly, the most stable structure was found to have the lowest PV contribution to H for each pernitride, except for baddeleyite-type IrN_2 and HgN_2, where the preferred structure was stabilized via the U term. Turning to $d_{\text{N-N}}$, it may be noticed that $d_{\text{N-N}}$ can be divided into two regions: the first five compounds (i.e., WN_2-PtN_2) have values that are closer to that of an N-N single bond (1.45 Å), while the latter two (i.e., AuN_2 and HgN_2) are closer to an N-N double bond (1.25 Å). Since all three structures of AuN_2 and HgN_2 are unstable, we focus on the first five compounds (i.e., WN_2-PtN_2). The formal oxidation states of the elements within these PmN_2 can be considered to be Pm^{4+} and N_2^{4-} [see Fig. 3(a)] [13]. More impressively, the fluctuation of $d_{\text{N-N}}$ correlates with an even/odd d-electron configuration in marcasite-type WN_2 (d^2), ReN_2 (d^3), OsN_2 (d^4), IrN_2 (d^5), and PtN_2 (d^6). This might be attributed to the fact that fewer d electrons are donated to N, which results in filling an antibonding level, when Pm^{4+} possesses an odd number of d electrons (d^3 and d^5) as opposed to an even number (d^2, d^4, and d^6), to maintain the symmetry of the degenerate electronic state of Pm^{4+}. Considering the aforementioned soft phonon mode in marcasite-type IrN_2 that leads to the marcasite-baddeleyite transition, it may be surprising that less electrons are donated to N_2 in this phase.

To solve this puzzle, COHP and electronic localization function (ELF) analyses were performed and the results are

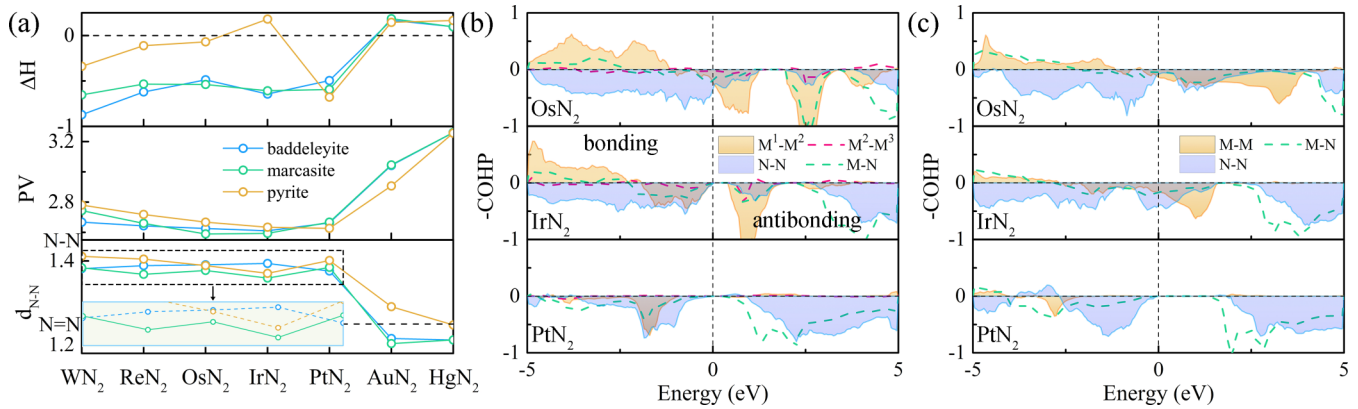

FIG. 2. (a) Calculated formation enthalpies ΔH (unit: eV/atom), PV term PV (unit: eV/atom), and bond lengths $d_{\text{N-N}}$ (unit: Å) of N-N pairs as a function of the transition metal in pernitrides assuming the baddeleyite, marcasite, and pyrite structures at 50 GPa. The inset shows an enlarged view for WN_2-PtN_2. (b), (c) Calculated COHP curves of (b) baddeleyite and (c) marcasite structures of OsN_2, IrN_2, and PtN_2.

shown in Figs. 2(b) and 2(c) and in Fig. S2 in Supplemental Material [30], respectively. It is seen in combination with Fig. 3(b) that the distortion leading to the marcasite-baddeleyite transition leads to Pm dimerization [10], which brings a sharp increase of the Pm-Pm integrated COHP [see the orange areas in Figs. 2(b) and 2(c) and in Table S2 in Supplemental Material [30]], and a distinctly delocalized electron distribution between Pm pairs in the ELF maps in baddeleyite-type OsN_2 and IrN_2. This indicates that the Pm-Pm bonding gradually weakens in going from OsN_2 to IrN_2 as the d-electron count increases, yet it is not observed in PtN_2. Pm dimerization results in a broadened d_{xy} band and narrowed $d_{x^2-y^2}$ band, as shown in Fig. 3(b), which can be used to quantify the extent of bonding and antibonding, respectively. Since the structural distortion has negligible effect on the other d states, marcasite-type OsN_2 and baddeleyite-type IrN_2

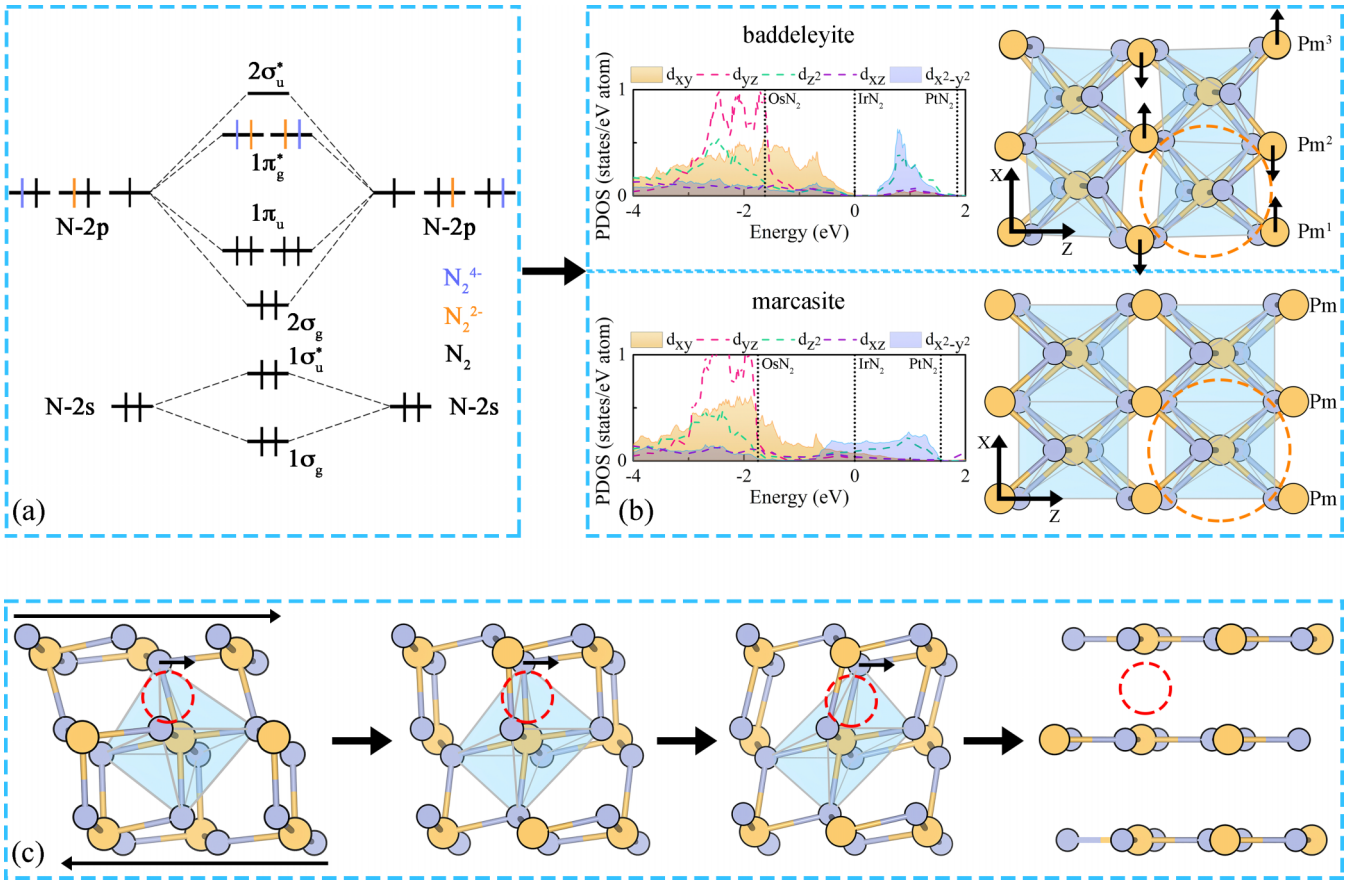

FIG. 3. (a) Qualitative molecular-orbital diagram of N_2 with different degrees of electron filling. (b) A comparison of a structural distortion diagram and partial density of states (PDOS) of baddeleyite- and marcasite-type structure. (c) An illustration of structural evolution of IrN_2 under shear strain along the weakest path.

TABLE I. Calculated Voigt polycrystalline bulk (B_V) and shear (G_V) moduli, Pugh ratio k [41], as well as calculated minimum ideal tensile ($\sigma_{\min}$) and shearing ($\tau_{\min}$) strength. The "Vickers hardness" (H_V^{Chen}) is provided according to the Chen *et al.* empirical hardness model [40].

	B_V (GPa)	G_V (GPa)	k	H_V^{Chen} (GPa)	Tension direction	$\sigma_{\min}$ (GPa)	Shear direction	$\tau_{\min}$ (GPa)	Ref.
Diamond	437	542	1.24	99.3	⟨111⟩	82.3	(111)⟨11$\bar{2}$⟩	86.8	[37,38]
c-BN	372	381	1.02	63.5	⟨111⟩	55.3	(111)⟨11$\bar{2}$⟩	58.3	[36,39]
ReB_2	348	274	0.79	37.3	⟨$\bar{1}$2$\bar{1}$0⟩	58.5	(0001)⟨10$\bar{1}$0⟩	34.4	[35]
OsN_2	369	241	0.65	27.1	⟨101⟩	42.1	(010)⟨101⟩	25.7	This paper
	359								[9]
IrN_2	342	221	0.65	25.2	⟨101⟩	26.1	(001)⟨ 100⟩	21.6	This paper
	354	224	0.63	24.8					[14]
PtN_2	286	203	0.71	27.0	⟨100⟩	28.4	(111)⟨$\bar{1}\bar{1}$2⟩	25.6	This paper
	288	221	0.77	31.5					[5]
	286	203	0.71	27.0	⟨100⟩	28.5	(111)⟨$\bar{1}\bar{1}$2⟩	25.5	[8]

are preferred due to the maximized filling of bonding (d_{xy}) and minimal filling of the antibonding ($d_{x^2-y^2}$) states, which lead to the anchoring effect of distorted octahedra. Whereas the Pm-N bond strength in these two structures is similar, as shown by the integrated COHP, the N-N bond strength is not. Pm dimerization results in a larger donation of electrons to the antibonding states in N-N, thereby leading to an increased N-N bond length [13], as illustrated in Fig. 2(a) and in Table S2 in Supplemental Material [30]. For baddeleyite-type OsN_2, a larger filling of the N-N antibonding states leads to a large density of states (DOS) at the Fermi level, which is typically a characteristic of unstable structures, whereas in marcasite-type IrN_2 a few electrons fill the N-N antibonding states, leaving a finite value near the Fermi level, thereby opening up a band gap [10]. In brief, N-N electron filling plays a destabilizing role in baddeleyite-type OsN_2 and marcasite-type IrN_2.

To understand the stabilization of PtN_2 in the pyrite structure at 50 GPa, ELF and COHP analyses were carried out. The results indicated that the Pm-Pm bonding induced by Pm dimerization in all three structures is weak and can be neglected (shown in Fig. S2 and Table S2 in Supplemental Material [30]). Although all three structures of PtN_2 are semiconductors (see Fig. S3 in Supplemental Material [30]), the largest band gap appears in the pyrite structure, suggesting that the hybridization between the Pm-d and N-p states is strongest in this structure. This indicates that the Pm-N bonding interaction plays a moderate role in the stabilization of pyrite-type PtN_2.

We next explore the elasticity and mechanical strengths of the most stable structures of IrN_2, OsN_2, and PtN_2 to determine if they may possess superior mechanical properties. Table I lists the calculated elastic properties of the pernitrides and several well-known hard or superhard materials [5,8,9,14,35–39]. It is seen that the three pernitrides show comparable bulk and shear moduli to those of superhard c-BN and ultraincompressible ReB_2, indicating their ultraincompressibility and high stiffness. According to the hardness model [40] based on elastic moduli G and Pugh's ratio k [41], i.e., $H_v = 2(k^2G)^{0.585} - 3$, OsN_2 is found to possess the highest bulk modulus (369 GPa) and hardness (27.1 GPa) among the three nitrides. However, it is generally accepted that plasticity descriptors should be included to get a more realistic quantification of plastic resistance or hardness [42]. Therefore, the ideal strength is evaluated. Table I lists the determined minimum ideal tensile and shear strengths along the weakest deformation path. Interestingly, the ideal shear strengths of the three pernitrides follow the trends of the hardness models: OsN_2 (25.7 GPa) possess the highest shear strength, which is followed by PtN_2 (25.6 GPa) and IrN_2 (21.6 GPa). All these values are much lower than those of hard ReB_2 (34.4 GPa) and superhard c-BN (55.3 GPa), ruling them out from the intrinsically superhard materials.

We finally explored the atomic deformation mechanism and electronic origin that intrinsically limits the mechanical strengths of the three pernitrides. Taking IrN_2 as an example, Fig. 4 illustrates the stress-strain curves and variation of Pm-N bond length during straining along the weakest deformation path. It is unexpected that the lattice instability originates from the breaking of the Pm-N bonds that elongate in the PmN_6 octahedra along specific shear deformation paths. Interestingly, no structural transformation is observed before approaching the critical strain, yet an anomalous variation appears for Pm-N bond lengths and stress. A similar creeplike behavior was observed in WB_4 under straining [43]. The loading process can be divided into four stages: S_0-S_1, S_1-S_2, S_2-S_3, and S_3-S_4, where S_0, S_1, S_2, S_3, and S_4 represent the equilibrium state, local stress maximum state, local stress minimum state, critical strain state, and lattice instability state, respectively. Noticeably, the transition point of anomalous change of the Ir-N1 distance, $d_{\text{Ir-N1}}$, begins exactly at S_1. Between S_1-S_2 both the stress and $d_{\text{Ir-N1}}$ decrease, then they increase during the S_2-S_3 stage. Almost the opposite trend is observed for $d_{\text{Ir-N2}}$. This suggests that the PmN_6 octahedron rotates at the S_1-S_3 stage [a schematic is shown in Fig. 3(c)], which affects the Pm-N bond lengths and redistributes charge. The latter can be identified by the deformed valence charge-density differences, as shown in Fig. 4. A positive (yellow color) or negative (cyan color) value indicates an accumulation (bond strengthening) or depletion (bond weakening) of charge, respectively. At S_1, the longer Ir-N1 bond has a stronger directional (covalent) charge distribution as compared to that of Ir-N2, which is accompanied by a strain-induced metal-semimetal transition revealed by the deformed electronic structure analysis (see

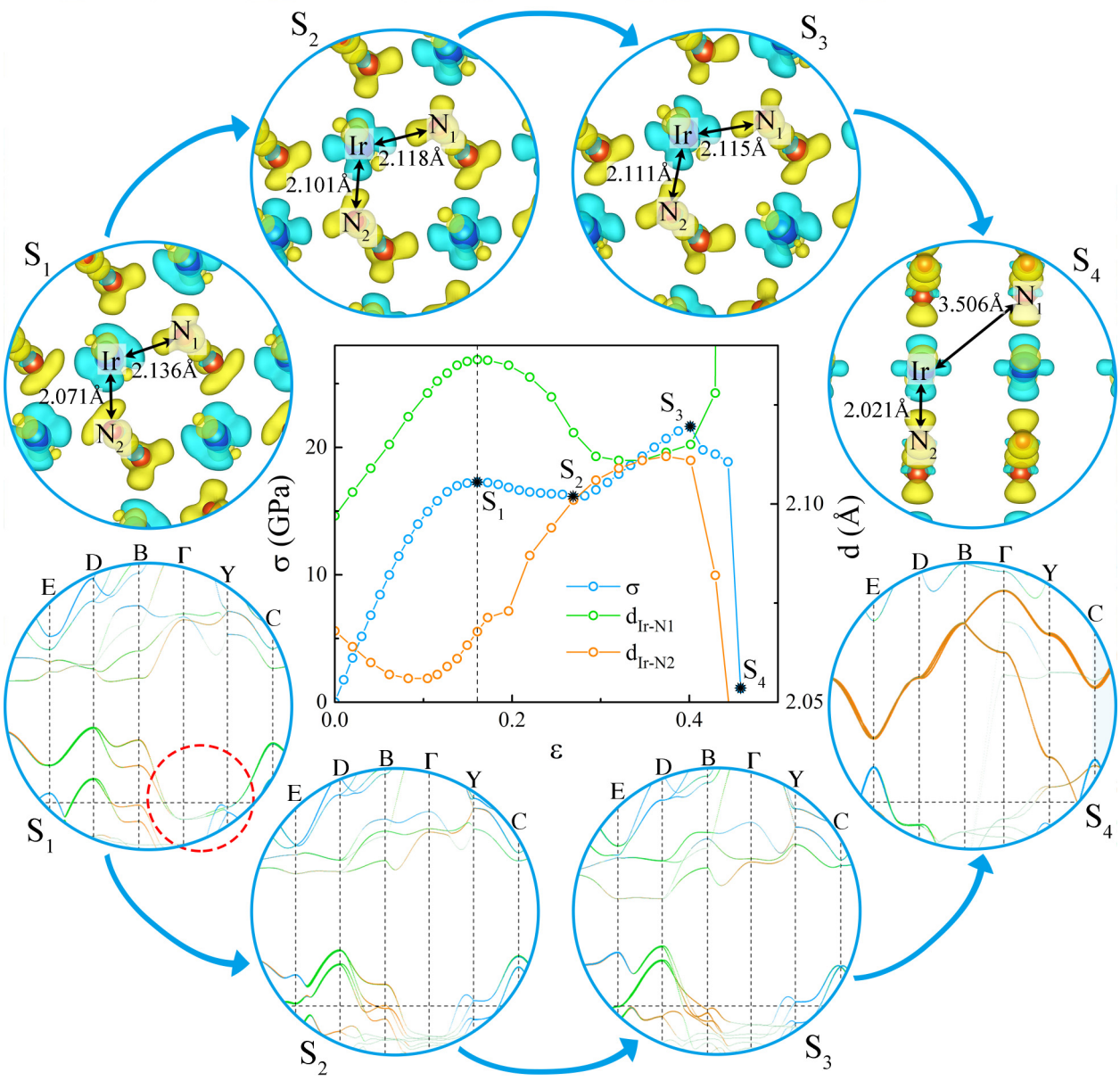

FIG. 4. The calculated stress σ and bond length $d_{\text{Ir-N}}$ vs strain ε curves of IrN_2 along the weakest shearing path. We selected four snapshots of the deformed orbital-resolved band structures and the valence charge-density differences (VCDD) under different shear strains to reveal the electronic origin. The orange, blue, and green colors represent three p orbitals of N, respectively. The isosurface of the VCDD corresponds to $\pm 0.022\, e^-/\text{bohr}^3$.

the lower panel for S_1 in Fig. 4). The bands composed of Pm-Pm antibonding states [see Figs. 2(b) and 3(b)] and a few N-p states (see the red circle in Fig. 4) move below the Fermi level along the high-symmetry line joining the Γ-Y points. The charge distribution between the Ir-N2 bonds shows an increasing directionality, and a semimetal-metal transition occurs as the strain increases at S_1-S_3. The bond length and charge distribution of Ir-N1 and Ir-N2 become similar at S_2-S_3. The narrow bands become dispersed with an increasing N-p state. From S_3 to S_4, the lattice is destabilized and the N-N bond length decreases sharply (1.36 to 1.27 Å), suggesting the formation of N-N double bonds at S_4. A similar anomalous variation appears for Os-N2 bond lengths and stress in OsN_2, while a metallic character remains during straining (see Fig. S4 in Supplemental Material [30]). Although a similar semiconductor-semimetal-metal transition also appears in PtN_2, a monotonic stress change and smaller critical strain suggest the brittle nature (see Fig. S5 in Supplemental Material [30]). In brief, the anchoring effect of distorted octahedra is responsible for the weakness of the pernitrides, in a similar manner to the role of Tm-N bonding widely observed in TmNs [15–17].

IV. CONCLUSIONS

In summary, two long-standing critical questions related to the stabilization of specific space groups and mechanical strengths for the platinum metal pernitrides are studied by

using high-throughput screening and evolutionary algorithms, orbital-resolved electronic structure analyses, and ideal strength calculations. Our results suggest that the stabilization of these pernitrides at high pressure cannot be simply understood by considering N-N bonding and Peierls distortions, but instead can be quantified by the anchoring effect of distorted PmN_6 octahedra via an orbital-resolved combinatorial strategy, which maximizes the stabilization (destabilization) effects derived from specific bonding (antibonding) interactions in specific crystal structures. The calculated plastic resistance and failure mechanism have unexpectedly ruled PmN_2 out of the intrinsically superhard materials because the weak Pm-N bonds in the distorted PmN_6 octahedra cause an electronic instability and plastic flow. These findings clarify the physical origin of high-pressure stabilization of PmN_2 and highlight the necessity to explore the atomic deformation mechanism in the design of novel strong solids.

ACKNOWLEDGMENTS

This work is supported by the National Key Research and Development Program of China (Grant No. 2016YFC1102500), National Natural Science Foundation of China (Grant No. 51672015), and National Thousand Young Talents Program of China. D.L. acknowledges support by the European Regional Development Fund in the IT4Innovations national supercomputing center Path to Exascale Project No. CZ.02.1.01/0.0/0.0/16_013/0001791 within Operational Programme Research, Development, and Education, by the Ministry of Education by Czech Science Foundation Project No. 17-27790S, and by Grant No. 8J18DE004 of Ministry of Education, Youth and Sport of the Czech Republic. E.Z. acknowledges the NSF (Grant No. DMR-1505817) for financial support. We would also like to thank Prof. G. Kresse for valuable advice for the application of VASP.

[1] E. Gregoryanz, C. Sanloup, M. Somayazulu, J. Badro, G. Fiquet, H.-k. Mao, and R. J. Hemley, Nat. Mater. **3**, 294 (2004).
[2] J. C. Crowhurst, A. F. Goncharov, B. Sadigh, C. L. Evans, P. G. Morrall, J. L. Ferreira, and A. J. Nelson, Science **311**, 1275 (2006).
[3] A. F. Young, C. Sanloup, E. Gregoryanz, S. Scandolo, R. J. Hemley, and H.-k. Mao, Phys. Rev. Lett. **96**, 155501 (2006).
[4] J. C. Crowhurst, A. F. Goncharov, B. Sadigh, J. M. Zaug, D. Aberg, Y. Meng, and V. B. Prakapenka, J. Mater. Res. **23**, 1 (2011).
[5] A. F. Young, J. A. Montoya, C. Sanloup, M. Lazzeri, E. Gregoryanz, and S. Scandolo, Phys. Rev. B **73**, 153102 (2006).
[6] D. Åberg, B. Sadigh, J. Crowhurst, and A. F. Goncharov, Phys. Rev. Lett. **100**, 095501 (2008).
[7] Z. T. Y. Liu, D. Gall, and S. V. Khare, Phys. Rev. B **90**, 134102 (2014).
[8] R. F. Zhang, D. Legut, Z. H. Fu, S. Veprek, Q. F. Zhang, and H. K. Mao, Phys. Rev. B **92**, 104107 (2015).
[9] J. A. Montoya, A. D. Hernandez, C. Sanloup, E. Gregoryanz, and S. Scandolo, Appl. Phys. Lett. **90**, 011909 (2007).
[10] R. Yu, Q. Zhan, and L. C. De Jonghe, Angew. Chem. Int. Ed. **46**, 1136 (2007).
[11] C. Z. Fan, J. Li, M. Hu, Z. S. Zhao, B. Xu, and J. L. He, J. Superhard Mater. **35**, 339 (2013).
[12] R. E. Peierls, *Quantum Theory of Solids* (Oxford University, New York, 1955).
[13] M. Wessel and R. Dronskowski, J. Am. Chem. Soc. **132**, 2421 (2010).
[14] Z. J. Wu, E. J. Zhao, H. P. Xiang, X. F. Hao, X. J. Liu, and J. Meng, Phys. Rev. B **76**, 054115 (2007).
[15] R. F. Zhang, S. H. Sheng, and S. Veprek, Appl. Phys. Lett. **94**, 121903 (2009).
[16] R. F. Zhang, Z. J. Lin, H.-K. Mao, and Y. Zhao, Phys. Rev. B **83**, 060101 (2011).
[17] R. F. Zhang, S. H. Sheng, and S. Veprek, Scr. Mater. **68**, 913 (2013).
[18] G. Kresse and J. Furthmüller, Comput. Mater. Sci. **6**, 15 (1996).
[19] P. E. Blöchl, Phys. Rev. B **50**, 17953 (1994).
[20] J. P. Perdew, K. Burke, and M. Ernzerhof, Phys. Rev. Lett. **77**, 3865 (1996).
[21] A. van de Walle and G. Ceder, J. Phase Equilib. **23**, 348 (2002).
[22] S. H. Zhang and R. F. Zhang, Comput. Phys. Commun. **220**, 403 (2017).
[23] A. Togo, F. Oba, and I. Tanaka, Phys. Rev. B **78**, 134106 (2008).
[24] R. Dronskowski and P. E. Bloechl, J. Phys. Chem. **97**, 8617 (1993).
[25] R. Hill, Proc. Phys. Soc. London, Sect. A **65**, 349 (1952).
[26] R. Hill, J. Mech. Phys. Solids **11**, 357 (1963).
[27] D. C. Lonie and E. Zurek, Comput. Phys. Commun. **182**, 372 (2011).
[28] D. C. Lonie and E. Zurek, Comput. Phys. Commun. **182**, 2305 (2011).
[29] A. Belsky, M. Hellenbrandt, V. L. Karen, and P. Luksch, Acta Cryst. B **58**, 364 (2002).
[30] See Supplemental Material at http://link.aps.org/supplemental/10.1103/PhysRevMaterials.3.013603 for the ICSD prototype library, calculated COHP integrated to the Fermi level, high-pressure phonon dispersions, and ELF maps of PmN_2; calculated partial density of states and COHP curves of PtN_2; and calculated stress and bond length versus strain curves of OsN_2 and IrN_2.
[31] S. Curtarolo, W. Setyawan, S. Wang, J. Xue, K. Yang, R. H. Taylor, L. J. Nelson, G. L. W. Hart, S. Sanvito, M. Buongiorno-Nardelli *et al.*, Comput. Mater. Sci. **58**, 227 (2012).
[32] J. E. Saal, S. Kirklin, M. Aykol, B. Meredig, and C. Wolverton, JOM **65**, 1501 (2013).
[33] Z. H. Wang, X. Y. Kuang, M. M. Zhong, P. Lu, A. J. Mao, and X. F. Huang, Europhys. Lett. **95**, 66005 (2011).
[34] W. Chen, J. S. Tse, and J. Z. Jiang, Solid State Commun. **150**, 181 (2010).
[35] R. F. Zhang, S. Veprek, and A. S. Argon, Appl. Phys. Lett. **91**, 201914 (2007).
[36] R. F. Zhang, S. Veprek, and A. S. Argon, Phys. Rev. B **77**, 172103 (2008).

[37] R. F. Zhang, Z. J. Lin, and S. Veprek, Phys. Rev. B **83**, 155452 (2011).
[38] H. Bu, M. Zhao, Y. Xi, X. Wang, H. Peng, C. Wang, and X. Liu, Europhys. Lett. **100**, 56003 (2012).
[39] A. Nagakubo, H. Ogi, H. Sumiya, K. Kusakabe, and M. Hirao, Appl. Phys. Lett. **102**, 241909 (2013).
[40] X. Q. Chen, H. Y. Niu, D. Z. Li, and Y. Y. Li, Intermetallics **19**, 1275 (2011).
[41] S. F. Pugh, Philos. Mag. **45**, 823 (1954).
[42] S. Veprek, J. Vac. Sci. Technol. A **31**, 050822 (2013).
[43] Q. Li, D. Zhou, W. Zheng, Y. Ma, and C. Chen, Phys. Rev. Lett. **115**, 185502 (2015).